JOM
https://doi.org/10.1007/s11837-024-06590-7

Oxidation Behaviour of Fe-28Al-5Si at.% Alloyed with Ti and Mo

ADAM HOTAŘ ,[1,4] VĚRA VODIČKOVÁ ,[1]
PETRA PAZOURKOVÁ PROKOPČÁKOVÁ ,[1] MARTIN ŠVEC ,[2]
PAVEL HANUS ,[1] and STANISLAV DANIŠ [3]

1.—Department of Material Science, Faculty of Mechanical Engineering, Technical University of Liberec, 46117 Liberec, Czech Republic. 2.—Department of Engineering Technology, Faculty of Mechanical Engineering, Technical University of Liberec, 46117 Liberec, Czech Republic. 3.—Department of Condensed Matter Physics, Faculty of Mathematics and Physics, Charles University of Prague, 121 16 Prague 2, Czech Republic. 4.—e-mail: adam.hotar@tul.cz

The high-temperature oxidation behaviour of Fe-28Al-5Si, Fe-28Al-5Si-2Mo and Fe-28Al-5Si-2Ti (in at.%) was investigated. Cyclic oxidation tests of iron aluminides were performed at 900°C and 1100°C. The oxidation kinetics and oxidation behaviour (by measuring of total weight gain, etc.) were described. The structure of the alloys' surfaces after oxidation, as well as the composition and morphology of oxide layers, was analysed by optical microscopy, scanning electron microscopy, SEM–EDS and X-ray diffraction. The beneficial effect of alloying with titanium or molybdenum on the oxidation resistance of Fe-Al-Si-based alloys was observed at temperatures of 900°C and 1100°C. Titanium and molybdenum suppress the formation of eutectic regions of the secondary phase in the structure, which preferentially oxidize. Therefore, a thin and compact alumina layer (only minor amounts of iron oxides and ZrO_2) formed on the surface of Fe-28Al-5Si-2Mo and Fe-28Al-5Si-2Ti at 900°C. These alloys maintain low weight gains even at a temperature of 1100°C. On the other hand, alloy Fe-28Al-5Si contains a high number of eutectics-like areas, which causes ingress of the oxidation (selective oxidation of eutectic areas) and breakaway oxidation is observed at 900°C and 1100°C, respectively.

INTRODUCTION

Since the 1950s, Fe-Al-based alloys have been developed as structural materials for high-temperature applications because of their very good resistance in many environments (e.g., oxidation, sulfidation atmosphere, etc.) and low feedstock cost. The aim was to replace high-alloyed steels containing deficient elements such as chromium and nickel.

For this reason, emphasis is placed on the improvement of the high-temperature mechanical properties by suitable alloying of Fe_3Al-based alloys. The strengthening of the Fe-Al matrix can be achieved by forming precipitates such as carbides and Laves phase.[1,2] Another possibility is strengthening due to the solid solution hardening by adding elements with high solubility in the matrix, e.g., silicon, chromium, etc.[3]

At present, attention is paid to the influence of Si and the combination of Si with other alloying elements on the mechanical properties of Fe-Al alloys produced by powder metallurgy and also by conventional casting.[4–9]

For alloys produced by reactive sintering or mechanical alloying and spark plasma sintering, the high-temperature oxidation behaviour has already been investigated in detail at 800°C and 1000°C.[4,7,10–12] First, Novák et al.[10] studied the effect of aluminium and silicon content on the oxidation behaviour of Fe-Al-Si alloys at 800°C produced by reactive sintering. The presence of silicon up to 20 wt.% leads to improvement of the oxidation resistance. Therefore, the alloys FeAl30Si10 and FeAl20Si20 (in wt.%) have lower weight gains than FeAl10Si30 (in wt.%). However, the lower oxidation resistance of FeAl10Si30 (in wt.%) may be due to increased porosity.[10]

(Received December 17, 2023; accepted April 8, 2024)

Published online: 17 May 2024

Ternary alloys FeAl35Si5 and FeAl20Si20 (in wt.%) were also produced by a combination of mechanical alloying and spark plasma sintering to achieve low structural porosity of the materials.[11] These alloys show a significantly lower oxidation rate at 800°C than binary alloys FeAl32 and FeSi14 (in wt.%). The oxide layer on ternary Fe-Al-Si alloys contains Al_2O_3 (θ-Al_2O_3 or γ-Al_2O_3) and a minor amount of Fe_2O_3 after oxidation at 800°C. In addition, SiO_2 was also found on the surface of the alloy FeAl20Si20 (in wt.%) because of the higher silicon content in the alloy. The alloy FeAl20Si20 (in wt.%) is again coated with aluminium oxide and a small amount of Fe_2O_3 and SiO_2 at the oxidation temperature of 1000°C.[7] However, allotropic modification of alumina occurs at the temperature of 1000°C. Instead of γ-Al_2O_3, α-Al_2O_3 is formed on the surface of FeAl20Si20 (in wt.%) during isothermal oxidation at 1000°C.

The effect of nickel and titanium on the cyclic oxidation behaviour of the FeAl35Si5 alloy at 800°C was also studied.[12] Nickel did not participate in the formation of oxides on the surface of the FeAl35-Si5Ni20 alloy and probably causes a reduction in the delamination of the oxide layer during the cyclic oxidation test. However, the addition of 20 wt.% Ti has a detrimental effect on the oxidation resistance of the FeAl35Si5 (in wt.%). In addition to γ-Al_2O_3 and Fe_2O_3, TiO_2 was also identified in the oxide layer. TiO_2 is porous and non-adherent to the surface, and therefore more extensive scale spallation was observed.

In the case of ternary Fe-Al-Si alloys manufactured by casting, the high-temperature oxidation behaviour has not been studied in detail yet. Therefore, the article aims to describe the effect of silicon and the combination of silicon with titanium or molybdenum on high-temperature oxidation at 900°C and 1100°C. The article pays attention to the oxidation kinetics, oxidation behaviour and analysis of oxide layers on the surface of Fe-28Al-5Si, Fe-28Al-5Si-2Ti and Fe-28Al-5Si-2Mo alloys (in at.%).

MATERIAL AND METHODS

The investigated alloys are summarised in Table I, in which the nominal composition of these alloys is also given. The alloys were produced from pure raw metals. The zirconium crucibles (zirconia material ZC93i) placed in a vacuum induction furnace were used to melt the alloys. After the melting, all alloys were cast into a rectangular metal mould. More details about the melting and casting of Fe-Al-Si alloys are given in Ref. 8.

Table I. Nominal chemical composition of tested alloys in at.%

Alloys	Fe	Al	Si	Mo	Ti	Zr
Fe-28Al-5Si	Bal.	28.0	5.0	–	–	0.2
Fe-28Al-5Si-2Mo	Bal.	28.0	5.0	2.0	–	0.2
Fe-28Al-5Si-2Ti	Bal.	28.0	5.0	–	2.0	0.2

Samples of 10 mm × 10 mm dimensions and 1 mm thickness were cut from the ingots by electrical discharge machining. All sides of the sample were ground to 1200 grit. Cyclic oxidation tests of alloys were performed at 900°C and 1100°C in laboratory air. The samples were first placed in alumina crucibles and then heated in a muffle furnace, which is fitted with the front and back inlet for airflow through the furnace. The heating rate of the samples was 10°C/min with a cooling rate of 2°C/min. During the oxidation test, each sample was weighed with the crucible to determine the total mass gain after 25 h, 50 h, 75 h, 100 h, 150 h, 200 h, 300 h, 400 h and 500 h. An electronic analytic balance with a precision of 10^{-4} g was used to weigh the samples.

The oxide layer on the alloys was first documented by optical microscopy (LOM) and scanning electron microscopy (SEM). The chemical and phase compositions of scales were analysed by Tescan Vega 3 SBH scanning electron microscope with Oxford Instruments X-Max 20 mm^2 (EDS) and X-ray diffraction (XRD) analysis. Panalytical X'Pert Pro MPD diffractometer employing Cu Kα radiation was used for XRD analysis. The diffractometer geometry was adapted to analyse thin oxide films. PCPDFWIN 2.4 ©2003 software with the list of JCPDS-ICDD cards was used for identifying the X-ray peaks. Attention was also paid to the documentation and analysis of the ingress oxidation; therefore, metallographic specimens were produced from the samples. Preparation of metallographic samples consists of careful cutting with a precision saw, encapsulating them into conductive resin, grinding with diamond suspensions and final polishing by a suspension of non-crystallizing colloidal silica.

RESULTS AND DISCUSSION

Microstructure of the Tested Alloys

The structure of the alloys used in the experiment has been already described in detail in connection with the high-temperature mechanical properties of these alloys.[8]

The coarse-grained structure of ternary alloy Fe-28Al-5Si shows a dendritic character with eutectics-like areas in inter-dendritic spaces.

According to XRD results, these eutectics-like areas are composed of Fe_3Al matrix and a mixture of very fine—in the order of hundreds of nanometres—zirconium carbides (or complex zirconium carbides, $Zr_3Al_3C_5$) and iron silicides (Fe_3Si); see Fig. 1a. The phase identification seems to be somewhat complicated because of multi-alloying. It can be expected that not only elements with limited solubility but also those with higher solubility in the matrix (Si) will also participate (under certain

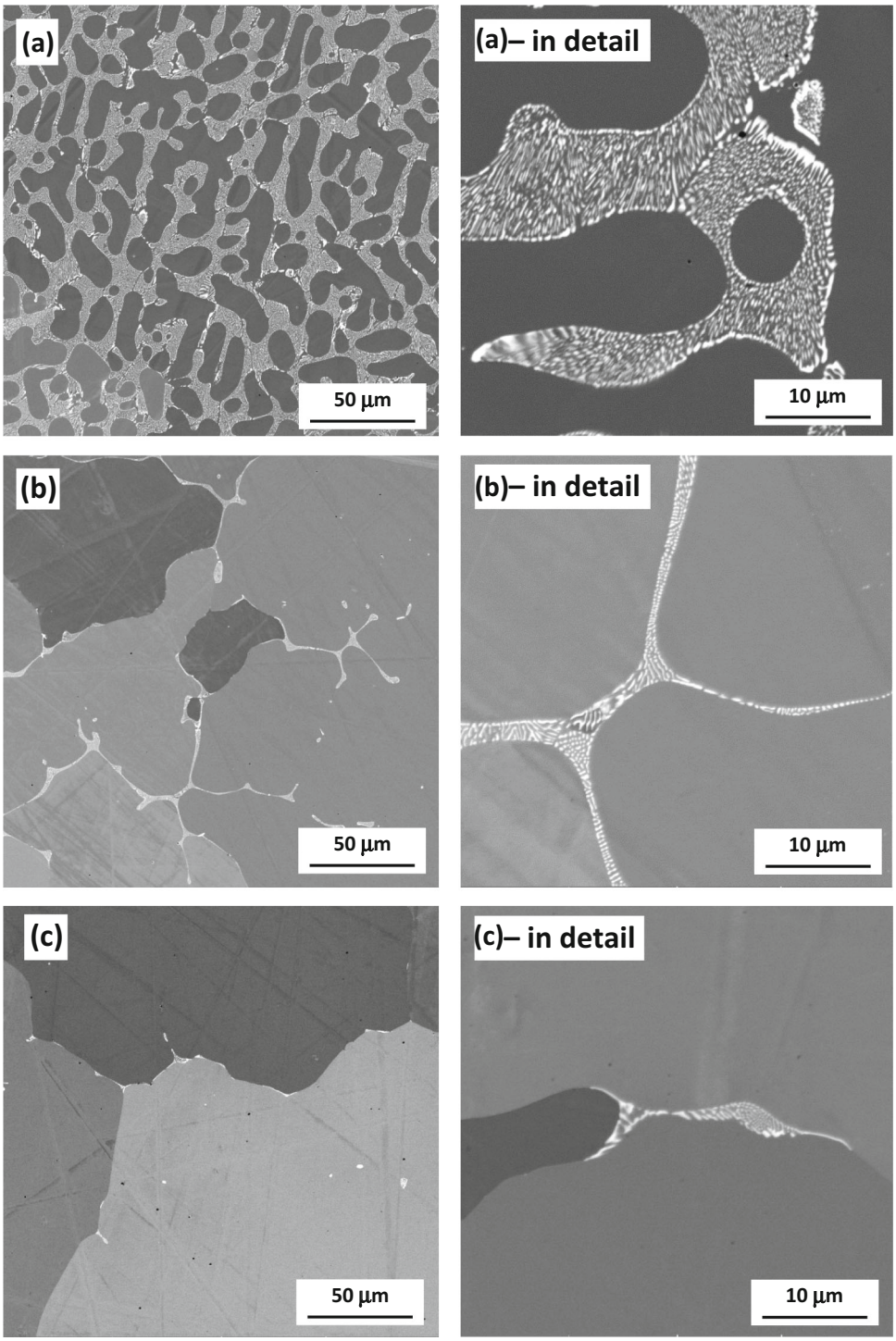

Fig. 1. Structures of tested alloys in the as-cast state: (a) Fe-28Al-5Si, (b) Fe-28Al-5Si-2Mo and (c) Fe-28Al-5Si-2Ti.

circumstances) in secondary phase formation. Primarily, the solubility is controlled by temperature—so the possibility of precipitation of the next secondary phase during the high-temperature and long-term cycle should be considered.

Both quaternary additives, molybdenum and titanium, influence the structure of ternary alloy significantly, first in terms of grain size and second in terms of the structure characterization (secondary phase distribution and possibly its composition).

In Fe-28Al-5Si-2Mo alloy, grains were noticeably finer compared to ternary alloy. Residual eutectic areas composed of Fe_3Al matrix and carbides similar to eutectics in alloy Fe-28Al-5Si were distributed only along grain boundaries (Fig. 1b).

Titanium addition obviously affects the grain size even more than molybdenum addition. There are equiaxed grains with dimensions of tens of micrometres in the case of Fe-28Al-5Si-2Ti alloy (Fig. 1c). Regarding phase composition, only a small part of added titanium contributes to the formation of secondary particles because of the high solubility of Ti in the Fe_3Al matrix. Residual eutectics-like areas composed of complex zirconium carbides of Si or Ti were rarely present at the grain boundaries.[8]

Oxidation Kinetics

The resistance to cyclic oxidation was tested for the ternary alloy as well as for Ti-alloyed and Mo-alloyed alloys (Fig. 2). At 900°C, the parabolic growth of weight gain has been observed in the case of Fe-28Al-5Si alloy; see Fig. 3. The weight gains for Fe-28Al-5Si-2Ti and Fe-28Al-5Si-2Mo alloys could not be recorded in Fig. 3 because of their extremely low values (in the range of 0.0001–0.0003 g), indicating excellent oxidation resistance. In this case, the weight gains were not possible to determine with sufficient credibility by analytical balance because the weight gain does not differ significantly from the weight measurement error (0.0001 g). Also, the oxidation kinetics at 1100°C of the tested alloys is given in Fig. 3. The total mass gains of Fe-28Al-5Si-2Ti and Fe-28Al-5Si-2Mo alloys follow the parabolic law (with minor deviations) at this high temperature (1100°C). In the case of Fe-28Al-5Si alloy, relatively low weight gains up to 200 h were measured, and then there was a significant oxidation acceleration especially from 300 h; see Fig. 3.

It was possible to calculate the parabolic rate constant only for alloys in which the oxidation demonstrably follows the parabolic law. These values for the tested alloys and other comparative alloys are summarised in Table II. The parabolic rate constant could not be calculated for Fe-28Al-5Si-2Ti and Fe-28Al-5Si-2Mo because the parabolic growth of the oxides could not be unambiguously confirmed because of the extremely low weight gain during oxidation at 900°C (as stated above). At a temperature of 900°C, the Fe-28Al-5Si alloy has a very low *kp* value, which is even slightly lower than *kp* of the Fe-25Al binary alloy.[13] This fact corresponds very well with the beneficial effect of Si on the oxidation behaviour of Fe-Al alloys at 800°C observed by Novák and Nová.[14] The alloys Fe-29.3Al-28.2Si (FeAl20Si20 wt.%) and Fe-50.9Al-7.0Si (FeAl35Si5 wt.%) exhibit a three to four order lower parabolic rate constant than Fe-49.3Al (FeAl32 wt.%) binary alloys.[14] It can be assumed that alloys alloyed by Ti and Mo also have low *kp* values. The beneficial effect of titanium or molybdenum alloying on the oxidation kinetics of alloy Fe-28Al-5Si is more pronounced at 1100°C. Fe-28Al-5Si-2Ti and Fe-28Al-5Si-2Mo alloys maintain low *kp* values at this high temperature, which are comparable to complex alloy Fe-29.7Al-3.8Cr-0.3Zr-0.2C (Table 2). On the other hand, Novák et al.[12] observed the detrimental effect of titanium on the oxidation resistance of Fe-50.9Al-7.0Si (FeAl35Si5 wt.%) at 800°C. Addition of 20 wt.% Ti to Fe-50.9Al-

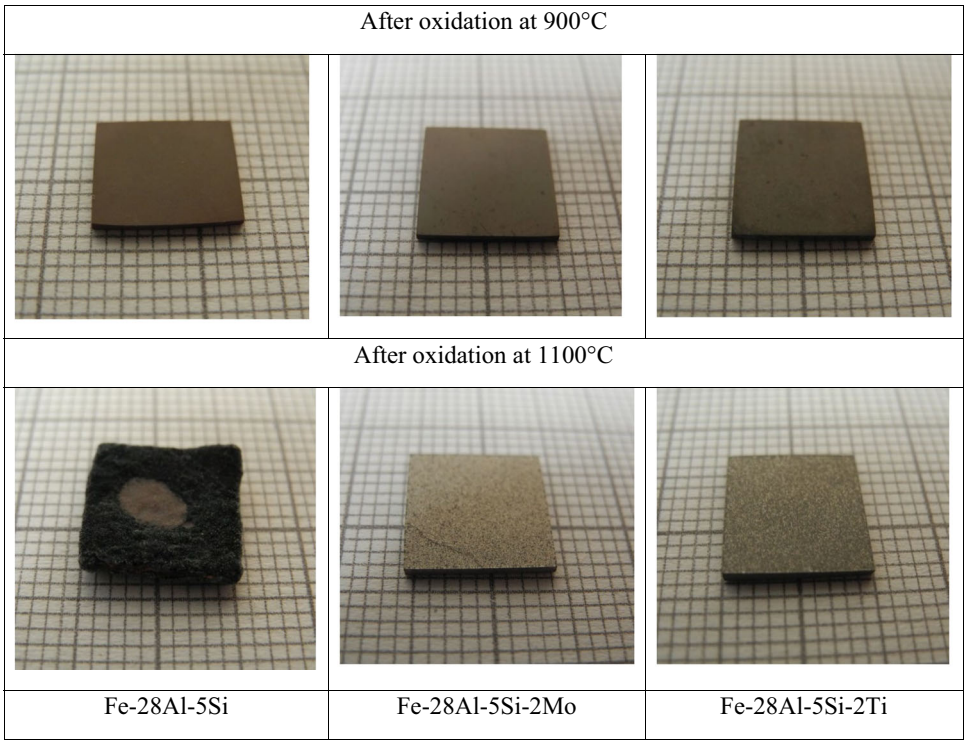

Fig. 2. Samples after cyclic oxidation in laboratory air.

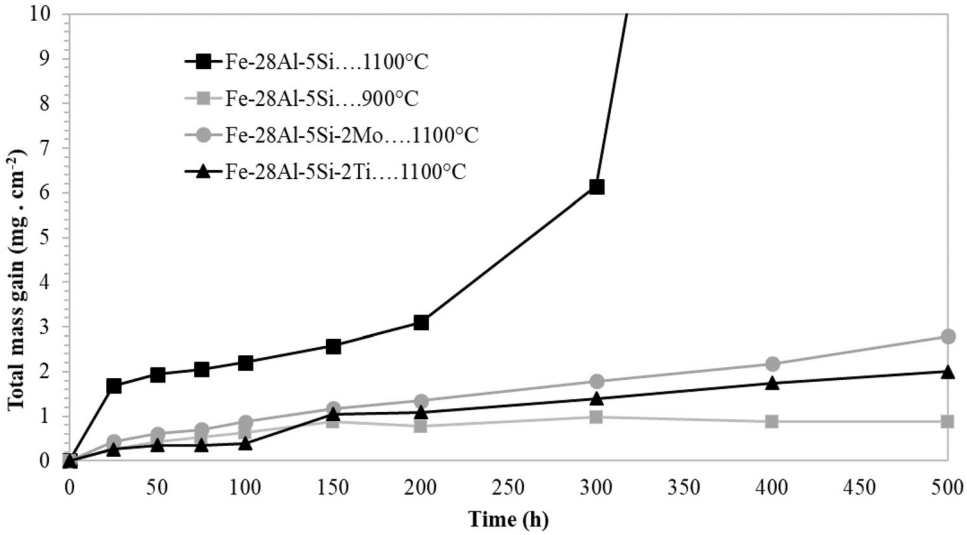

Fig. 3. Dependence of total mass gain on time during cyclic oxidation. [The weight gains for Fe-28Al-5Si-2Ti and Fe-28Al-5Si-2Mo alloys could not be recorded because of their extremely low values (in the range of 0.0001–0.0003 g) indicating excellent oxidation resistance.]

Table II. Apparent parabolic rate constant k_p after the cyclic oxidation test; the data for k_p were calculated in the range of 200–500 h

	k_p ($g^2\ cm^{-4}\ s^{-1}$)				
Alloy (at.%)	**800°C**	**900°C**	**1000°C**	**1100°C**	**References**
Fe-28Al-5Si	–	8.3×10^{-14}	–	y	This work
Fe-28Al-5Si-2Mo	–	x	–	2.7×10^{-12}	This work
Fe-28Al-5Si-2Ti	–	x	–	5.4×10^{-12}	This work
Fe-29.3Al-28.2Si FeAl20Si20 (wt.%)	2.6×10^{-13a}	–	7.2×10^{-13a}	–	11
Fe-50.9Al-7.0Si FeAl35Si5 (wt.%)	1.9×10^{-14a}	–	–	–	12
Fe-49.7Al-6.8Si-16.0Ti FeAl35Si5Ti20 (wt.%)	8.1×10^{-14a}	–	–	–	12
Fe-25Al	–	1.0×10^{-13b}	–	–	13
Fe-27Al-5Nb	–	6.7×10^{-13}	–	–	15
Fe-29.7Al-3.8Cr-0.3Zr-0.2C	–	8.3×10^{-14c}	7.5×10^{-13c}	2.7×10^{-12c}	16

x The parabolic rate constant could not be calculated.y No parabolic oxidation behaviour.[a]Calculated in the range of 0–400 h.[b]Isothermal oxidation, omitting the initial oxidation stage; the range is unknown.[c]Isothermal oxidation, omitting the initial oxidation 200 h.

7.0Si alloy (FeAl35Si5 wt.%) caused multiple increases in the parabolic rate constant; see Table II.

Oxide Analysis

The composition of oxide layers (supported by EDS chemical analysis results) was verified by XRD phase diffraction analysis (Figs. 4, 5, Tables III, IV).

After oxidation at 900°C, α-Al_2O_3 oxide (alpha modification, rhombohedral) was predominantly identified on the surface of Fe-28Al-5Si alloy. As the second phase, Fe_2O_3 oxide was determined. As another—the minority—phase, Fe_3O_4 and ZrO_2 oxides were present; see the diffractogram in Fig. 4.

The surfaces of alloyed alloys were covered by α-Al_2O_3 oxide almost solely; only small amounts of other oxides were recorded. In the case of Fe-28Al-5Si-2Ti alloy, Fe_2O_3 oxide and ZrO_2 oxide were both present in very small amounts. In the case of the oxide layer on Fe-28Al-5Si-2Mo alloy, except α-Al_2O_3, the minority oxides Fe_2O_3, Fe_3O_4 and ZrO_2 were recorded.

The formation of α-Al_2O_3 at 900°C on the matrix of tested alloys may also be affected by the presence of alloying elements. All tested alloys contain small amounts of zirconium, which belongs to the reactive elements. As is already known, reactive elements improve the adhesion of oxide layers and catalyse the transformation of θ-Al_2O_3 to α-Al_2O_3.[17–19] Even the silicon presence, in this case, can accelerate the

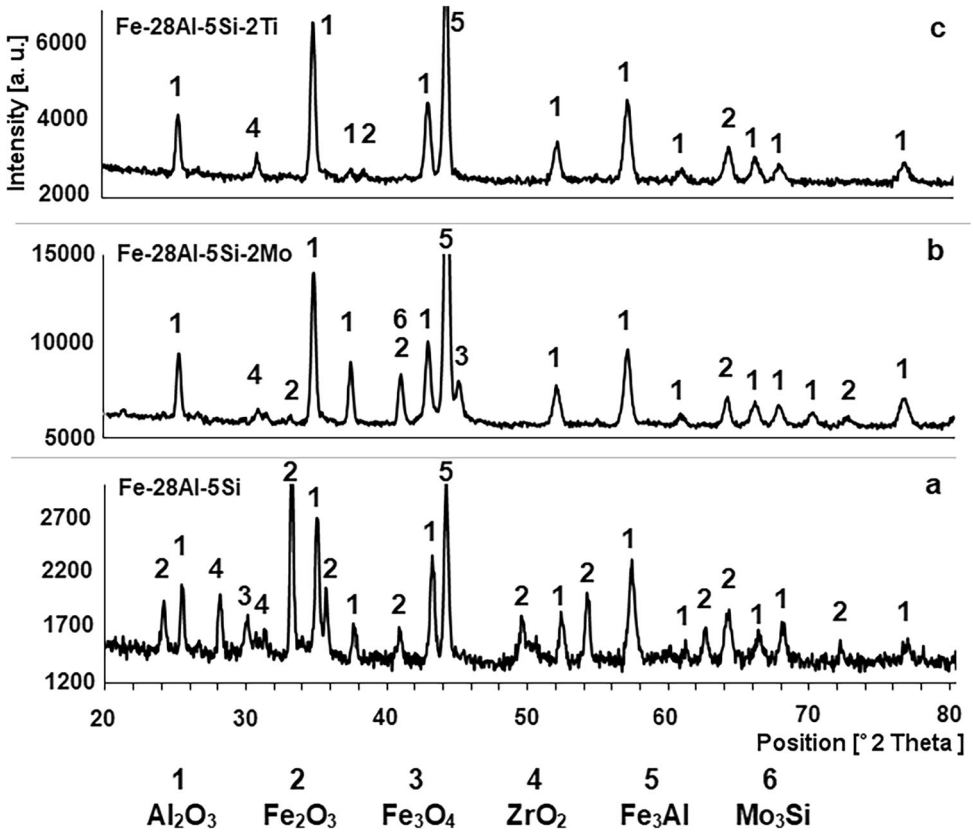

Fig. 4. X-ray diffractograms of (a) Fe-28Al-5Si, (b) Fe-28Al-5Si-2Mo and (c) Fe-28Al-5Si-2Ti after oxidations at 900°C.

transformation of the alumina metastable phase to a stable one.[20] Jamnapara et al. assume that silicon blocks the outward diffusion of cations (Al^{3+}) and thus promotes the formation of the α-Al_2O_3 layer.

Regarding the oxidation at 1100°C, the phase composition of the oxide layer on the surface Fe-28Al-5Si alloy was similar to this at the lower temperature, but with a different representation of oxides: Fe_2O_3 as majority phase, α-Al_2O_3 as the second phase, Fe_3O_4 and ZrO_2 in the lower quantities. On the other hand, the phase composition of layers on the surfaces of Ti- and Mo-alloyed alloys was much more homogeneous (that means homogeneous only in terms of phase composition), as seen from the comparison of diffractograms in Fig. 5. The oxide layer is obviously homogeneous on Fe-28Al-5Si-2Ti alloy, and only α-Al_2O_3 oxide was identified. The oxide layer on Fe-28Al-5Si-2Mo alloy is also homogeneous in terms of composition; the Mo_3Si phase occurs as the secondary phase in the alloy structure.

Post-mortem investigation of oxide layers after oxidation at 900°C shows that the oxide layers on the surface of Ti- and Mo-alloyed alloys are thin and compact; see Fig. 6b, c. The adhesion of the oxide layer is very good for both alloys because scale spallation was not observed. The surface of Fe-28Al-5Si alloy is covered with a greater thickness of oxides than alloys with the addition of Ti and Mo; compare Fig. 6a, b, c. The increase in temperature to 1100°C was reflected in an increase in the thickness of the oxide layer, as shown by the increased weight gain (Fig. 3) and cross-section image (Fig. 7). After oxidation tests at 1100°C, the oxide layer does not cover the whole surface of the samples because the scale spalling occurs during the oxidation test (Fig. 7b, d). The scale spalling was more pronounced in the case of Fe-28Al-5Si-2Mo alloy (Fig. 7b). It can be assumed that during cyclic temperature changes, the cracking and spalling of the Al_2O_3 layer occurs because of thermal stress between the oxide layer and the matrix. Precipitation of Mo_3Si (bright particles, Figs. 7b, 8) can also cause spalling of the oxide layer. Similarly, the spallation of oxides from the surface of the alloy Fe-25Al-2Ta after oxidation at temperatures of 900°C and 1000°C was explained.[21] In this case, they precipitated Fe_2Ta particles under the oxide layer.

For a better idea of the way oxides distribute on the surface, the oxide layers were also investigated by energy-dispersive X-ray spectroscopy. The mapping of elements (Fig. 9) shows that the distribution of oxides corresponds to the shape and size of the secondary phases, which occur in the alloys (Fig. 1). The difference is most noticeable on the surface of the Fe-28Al-5Si alloy (Fig. 1a): the thinner α-Al_2O_3

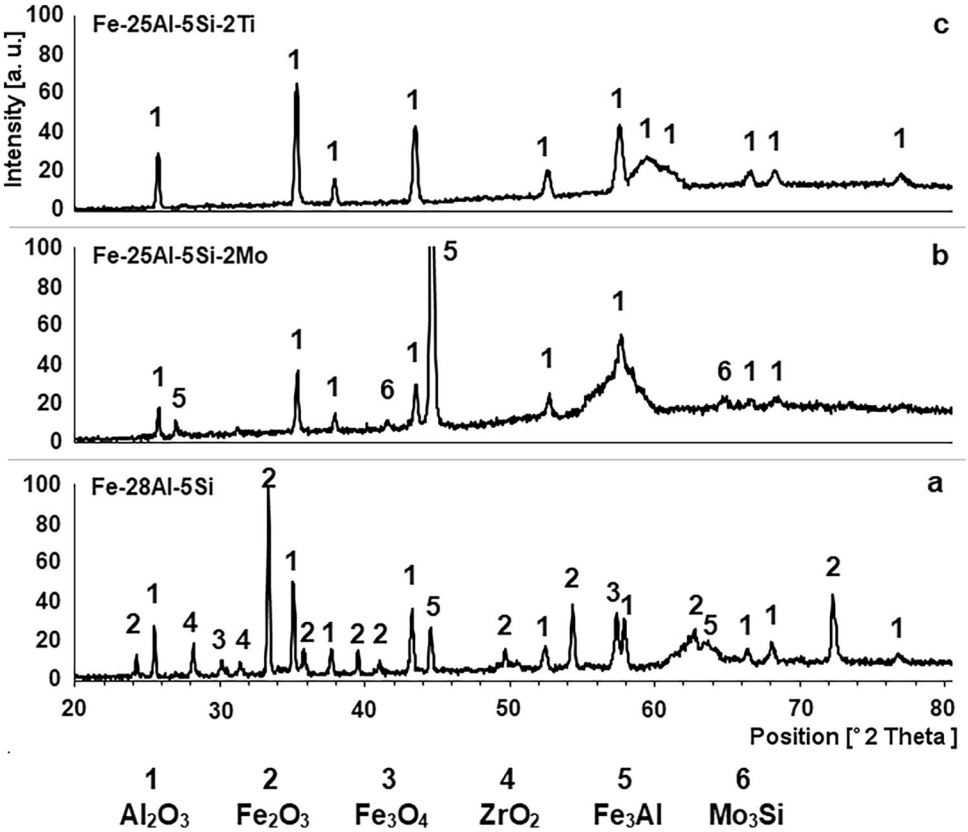

Fig. 5. X-ray diffractograms of (a) Fe-28Al-5Si, (b) Fe-28Al-5Si-2Mo and (c) Fe-28Al-5Si-2Ti after oxidations at 1100°C.

Table III. Crystallographic parameters of phases on the sample surfaces

Phase	PDF card	Space group	Crystal system
α-Al_2O_3 (corundum)	#89-3072	R-3c (167)	Rhombohedral
α-Fe_2O_3 (hematite)	#89-0596	R-3c (167)	Rhombohedral
Fe_3O_4 (magnetite)	#89-0951	Fd-3m (227)	Cubic
ZrO_2	#65-2357	$P2_1/c$ (14)	Monoclinic
Mo_3Si	#76-1577	Pm-3n (223)	Cubic
Fe_3Al	#65-5188	Fm-3m	Cubic

Table IV. Phase composition of the oxide layer formed on alloys, analysed by XRD and EDS

	Oxidation at 900°C/500 h	Oxidation at 1100°C/500 h
Fe-28Al-5Si	α-Al_2O_3, Fe_2O_3, minor amounts of ZrO_2, Fe_3O_4	Predominates Fe_2O_3, α-Al_2O_3, few Fe_3O_4, ZrO_2
Fe-28Al-5Si-2Mo	α-Al_2O_3, minor amounts of Fe_2O_3, Fe_3O_4, ZrO_2	Discontinuous oxide layer of α-Al_2O_3
Fe-28Al-5Si-2Ti	Predominates α-Al_2O_3, minor amounts of Fe_2O_3, ZrO_2	Discontinuous oxide layer of α-Al_2O_3

layer covers the Fe_3Al matrix while more voluminous oxides (composed of Fe_2O_3 predominantly) are located on the eutectics-like areas. On the other hand, the thinner α-Al_2O_3 layer on the surface of the Ti-alloyed and Mo-alloyed alloys appears more compact, with only minor "islets" (small areas) of Fe_2O_3 (Fig. 1b).

The presence of α-Al_2O_3 on the matrix is also possible to confirm by observation of the morphology oxide layer. After oxidation of Fe-28Al-5Si-2Ti at 900°C, the presence of α-Al_2O_3 on the matrix is also confirmed by the characteristic morphology of the oxide grains, which are fine and equiaxed; see details in Fig. 10c. Similar grains were observed

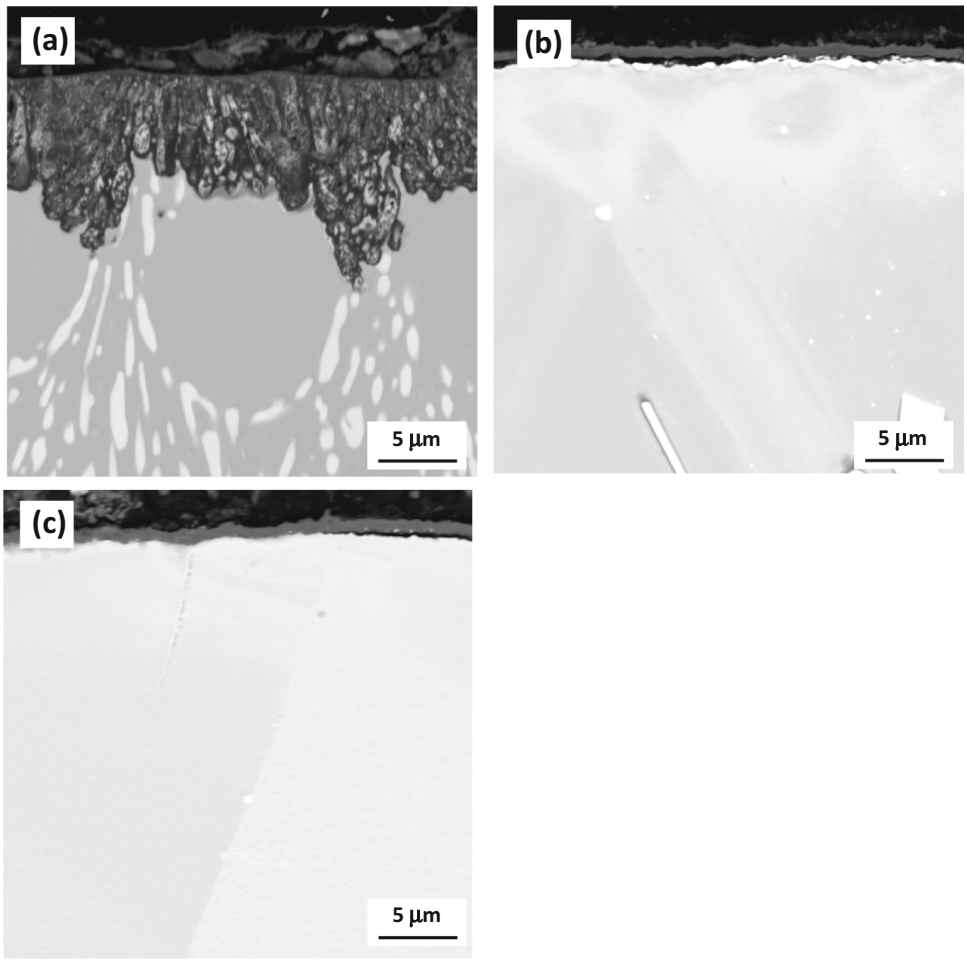

Fig. 6. Oxide layer on the alloys after oxidation at 900°C: (a) Fe-28Al-5Si, (b) Fe-28Al-5Si-2Mo and (c) Fe-28Al-5Si-2Ti.

on Fe-29.2Al (Fe-15Al in wt.%) after oxidation at 700°C/300 min[22] and also after cyclic oxidation of Fe-27Al-0.8Nb at 750°C/550 h.[23] The oxide layer on the surface of the Fe-28Al-5Si-2Mo contains not only equiaxed grains of Al_2O_3 but also a small amount of alumina plate-like grains (Fig. 10b). The Al_2O_3 layer on the Fe-Al matrix of the Fe-28Al-5Si has an indistinct fine morphology; only coarser equiaxed grains can be found in some places (Fig. 10a).

Different morphology of α-Al_2O_3 was observed on Fe-28Al-5Si-2Mo and Fe-28Al-5Si-2Ti alloys after cyclic oxidation at 1100°C/500 h (Figs. 11, 12). A fractured cross section of the alumina oxide layer on Fe-28Al-5Si-2Mo shows that columnar grains are present near the metal/oxide interface. The upper part of the oxides (near interface oxide/air) consists of plate-like grains. Observation of the morphology of α-Al_2O_3 oxides on Fe-28Al-5Si-2Ti revealed that columnar grains again occur near the alloy/oxide interface. A layer of alpha alumina with a network-like structure was formed on the columnar grains of α-Al_2O_3 (Fig. 12). A similar morphology of α-Al_2O_3 was also observed on NiAl[24] and NiAl-Zr alloys[25] after one week of oxidation at 1100°C and after 100 h at 1100°C, respectively.

Compared to Mo- and Ti-alloyed alloys, a completely different oxidation behavior was recorded in the case of Fe-28Al-5Si alloy. Significant initial oxidation was already observed at an oxidation temperature of 900°C (Fig. 6a). The eutectic, which becomes significantly coarser because of the high temperature during oxidation test duration, oxidizes preferentially; see Fig. 13. The eutectic mixture is composed of Fe_3Al matrix and secondary phase particles again but the chemical composition of these coarse particles is slightly different: compared to the state before the long-term oxidation test, the silicon content was noted in complex carbides by means of SEM–EDS mapping (Fig. 13)

Although two types of secondary phase ($Zr_3Al_3C_5$ and Fe_3Si) were identified by XRD analysis in the structure of origin Fe-28Al-5Si alloy (before the test),[8] the formation of other complex carbides on the Si-Zr base during the oxidation test is not out of the question (provided that aluminum atoms could be partially substituted by silicon atoms in these carbides because of decreasing solubility of silicon in Fe_3Al matrix with increasing temperature).[26,27]

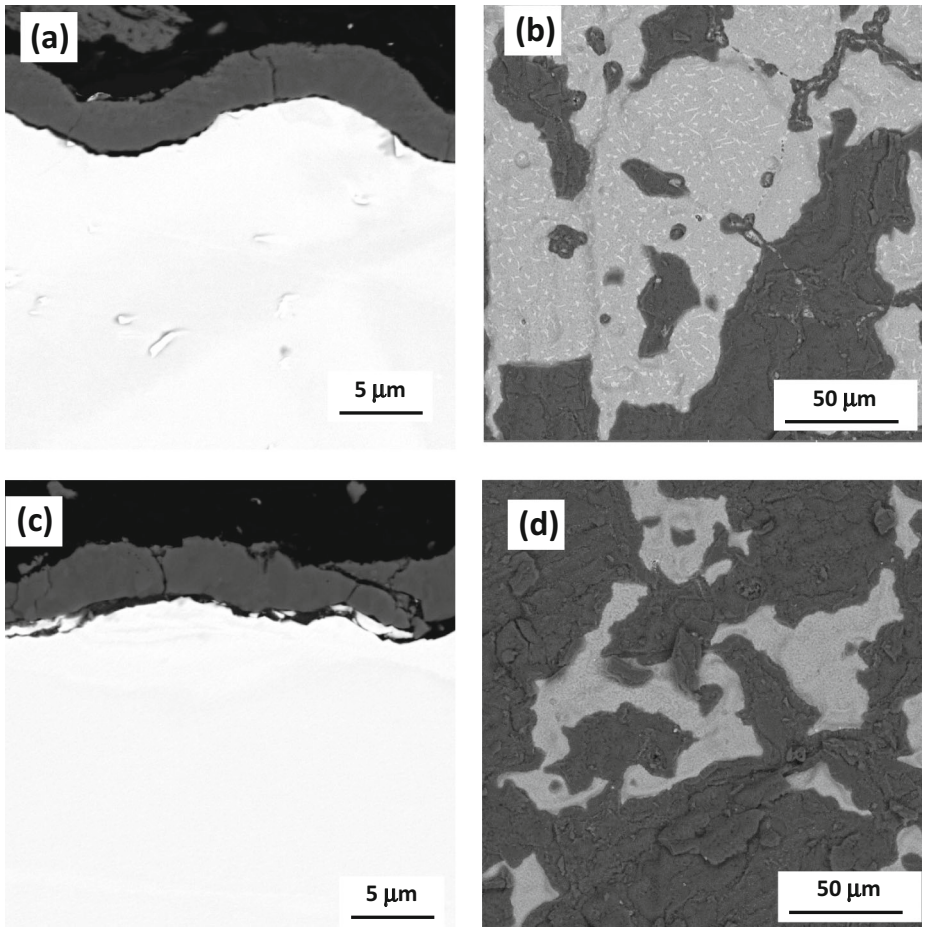

Fig. 7. Oxide layer on the alloy surface after oxidation at 1100°C: (a) Fe-28Al-5Si-2Mo, cross section, (b) Fe-28Al-5Si-2Mo, surface (bright = matrix, grey = Al_2O_3), (c) Fe-28Al-5Si-2Ti, cross section and (d) Fe-28Al-5Si-2Ti, surface (bright = matrix, grey = Al_2O_3).

During oxidation, the mixture of Al_2O_3, ZrO_2, Fe_3O_4 and Fe_2O_3 forms at the place of eutectic occurrence (Figs. 4, 13). Figure 13 shows the matrix is passivated by Al_2O_3. The presence of "a cap" formed by Fe_2O_3 oxide is evident on the surface of the oxide protrusion. This fact corresponds well with SEM–EDS element mapping of the surface (Fig. 9). The presence of ZrO_2 during the initial oxidation can be explained by the reaction of precipitates $Zr_3Al_3C_5$ with air, similar to the oxidation of the $Zr_3Al_3C_5$ powder published in Ref. 28. Subsequently, ZrO_2 will probably be formed mainly by the oxidation of complex carbides on the Si-Zr base.

At 1100°C after 200 h of oxidation, the breakaway oxidation of Fe-28Al-5Si occurs; see Fig. 3. The surface of the alloy is not covered with a protective alumina layer; the volume and non-protective Fe-based oxides predominate here (on the surface). The presence of mainly Fe_2O_3 and also Fe_3O_4 on the surface of the alloy was already confirmed by XRD analysis (Fig. 5). The sample's surface is mainly covered with oxides with a whisker-like morphology; only in the middle is there an area with a relatively smooth surface (Figs. 2, 14). Based on the XRD analysis, it can be assumed that this oxide with a whisker-like morphology is hematite (Fe_2O_3). In addition, a similar morphology of Fe_2O_3 was observed on iron aluminide coatings (Fe-40Al-0.05Zr at.%) after 36 h of oxidation at 1100°C.[29] Contrarily, a mixture of aluminium, iron and zirconium oxides is found on the smooth region's surface in the sample's centre (Fig. 14).

DISCUSSION

The oxidation behaviour of Fe-28Al-5Si, Fe-28Al-5Si-2Ti and Fe-28Al-5Si-2Mo has been evaluated at 900°C and 1100°C. The oxidation kinetics of alloys were described by the total mass gain. The phase and chemical composition of the oxide layer were analysed post-mortem using XRD, SEM and SEM–EDS.

The oxidation resistance of the tested alloys is significantly influenced by their as-cast structure, which is determined by the quaternary additives Ti and Mo. Additives Mo and Ti in alloys based on Fe-Al-Si affect the phase composition of alloys and grain sizes.

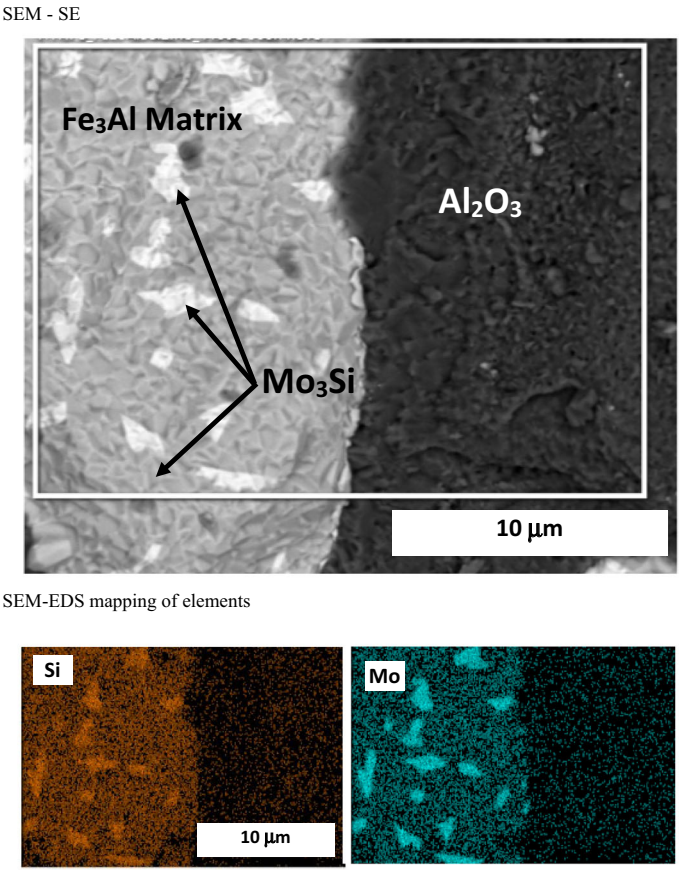

Fig. 8. SEM micrographs of surface of Fe-28Al-5Si-2Mo after oxidation at 1100°C/500 h.

Both additives, Ti and Mo, suppress the formation of eutectic areas (mixture of $Zr_3Al_3C_5$, Fe_3Si and Fe_3Al) that oxidize preferentially, as was shown for Fe-28Al-5Si alloy. The low frequency of appearance of eutectic regions and the predominance of the Fe_3Al matrix caused Fe-28Al-5Si-2Ti and Fe-28Al-5Si-2Mo alloys to be covered with a very thin layer of alumina at a temperature of 900°C. A mixture of voluminous oxides (iron oxides and ZrO_2) was formed on the surface only in places of eutectic regions. For the Fe-28Al-5Si alloy, where the presence of the eutectic regions is significantly more frequent, a thicker layer of oxides was formed on the surface, composed not only of Al_2O_3 but also of a large amount of Fe_2O_3 and other oxides. Additionally, ingress of oxidation into the alloy was observed in the eutectic regions. At a temperature of 1100°C, the detrimental effect of eutectic regions on oxidation resistance became even more pronounced. Therefore, alloy Fe-28Al-5Si was not covered by the protective alumina layer after 200 h, and breakaway oxidation occurred. Contrarily, for alloys alloyed with Ti and Mo, the thickness of Al_2O_3 increased slightly, which is evidenced by the low total weight gain. In both cases (Fe-28Al-5Si-2Ti and Fe-28Al-5Si-2Mo alloys) scale spalling was observed but was more significant on the surface of the alloy alloyed with Mo. Both these alloys showed approximately parabolic oxidation behaviour.

However, differences in grain size of tested alloys should be considered. Both elements, molybdenum and titanium, have been recorded as additives leading to grain refinement of various aluminium-based materials.[30] The effect of Mo directly on the metallurgical properties of cast iron aluminides has been investigated in detail in the past. It was determined that the addition of molybdenum results in a decrease in grain size in the case of Fe_3Al-based alloy doped by titanium boride.[31]

It can be assumed that the grain refinement of the Fe-28Al-5Si alloy was just caused by titanium and molybdenum alloying (usually, this aspect is also crucial for maintaining the mechanical properties). Then, the fine-grained structure in combination with a low number of eutectic regions improves the high-temperature corrosion resistance of Fe-28Al-5Si-2Ti and Fe-28Al-5Si-2Mo in air.

The grain size can become an important parameter in the case of solid solutions if the grain boundary is a weak point of its structure, so the corrosion attack penetrates deeper for bigger grains.[32] On the other hand, the corrosion resistance of fine-grained structures can be lower if a

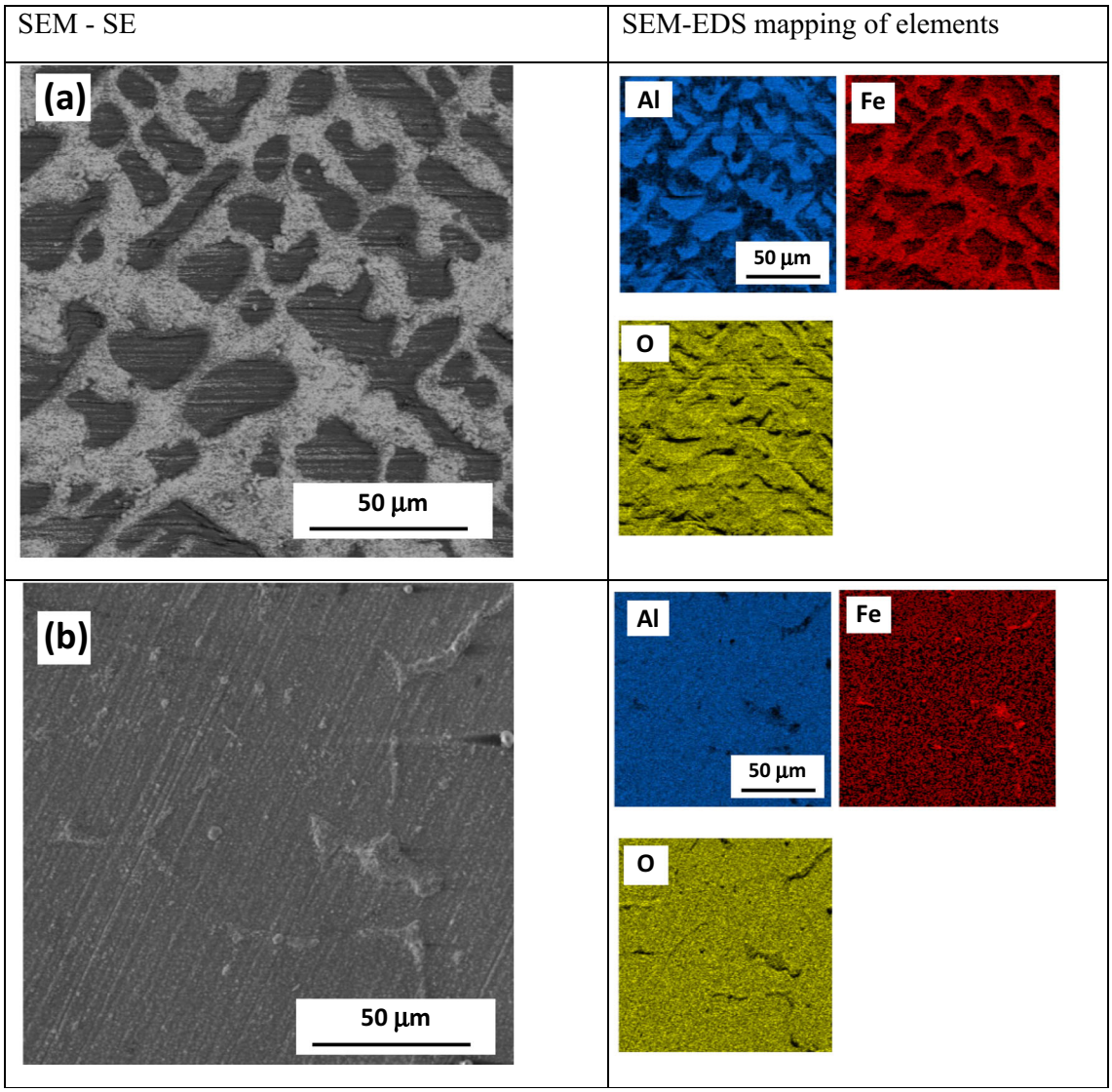

Fig. 9. SEM micrographs of oxides on alloy surfaces after oxidation at 900°C/500 h: (a) Fe-28Al-5Si, (b) Fe-28Al-5Si-2Mo.

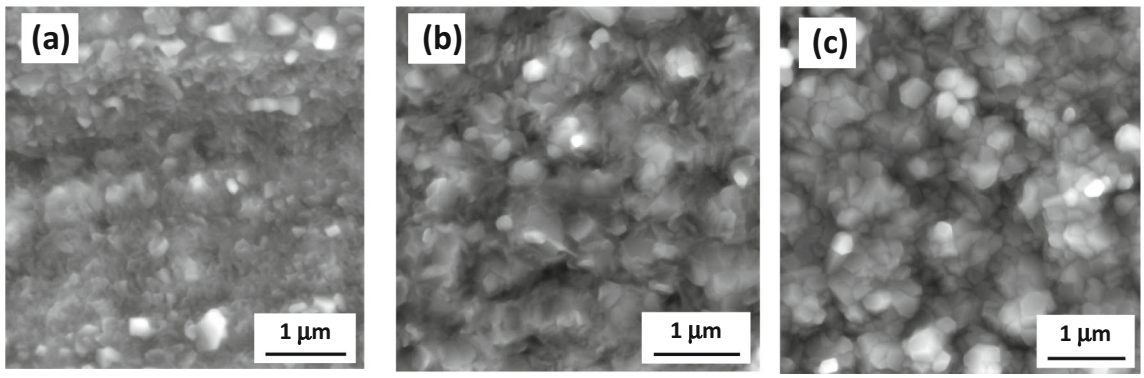

Fig. 10. Oxide grains on the matrix of alloys after oxidation at 900°C/500 h: (a) Fe-28Al-5Si, (b) Fe-28Al-5Si-2Mo, (c) Fe-28Al-5Si-2Ti.

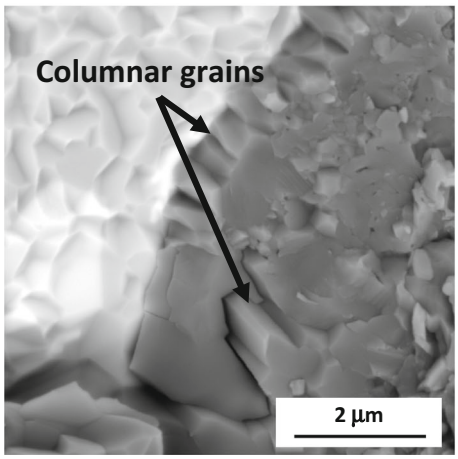

Bright part – matrix, grey part – alumina oxides

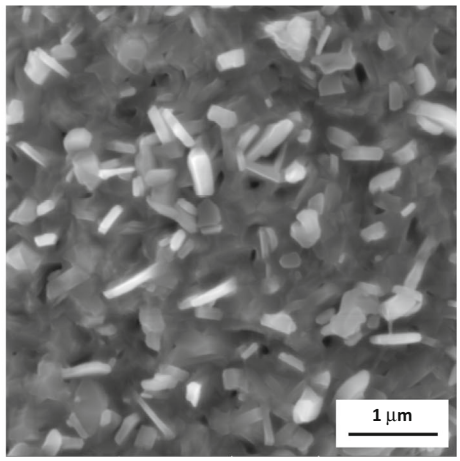

plate-like grains near interface oxide/air

Fig. 11. Morphology of alumina oxide on alloy Fe-28Al-5Si-2Mo after oxidation at 1100°C/500 h.

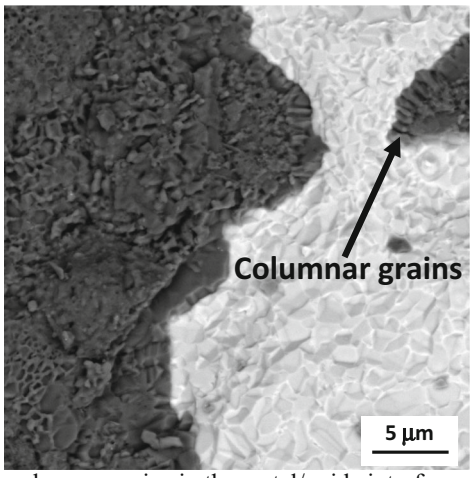

columnar grains in the metal/oxide interface

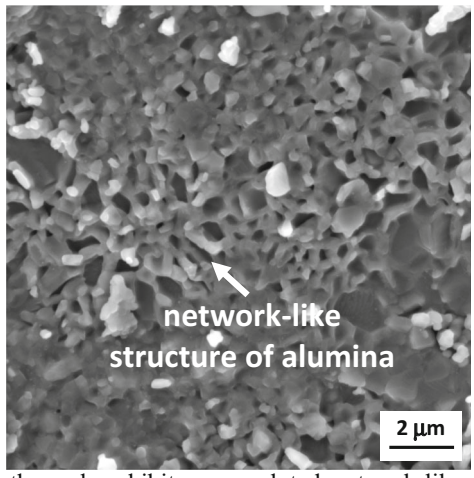

the scale exhibits a convoluted, network-like structure

Fig. 12. Morphology of alumina oxide on alloy Fe-28Al-5Si-2Ti after oxidation at 1100°C/500 h.

higher percentage of preferentially oxidizing secondary phases is distributed at the grain boundaries.[33]

It can be summarized that both additives, Ti and Mo, affect the phase composition of alloys by suppressing the formation of eutectic areas that oxidize preferentially, as was shown for Fe-28Al-5Si alloy. The differences in the composition of oxide layers covering the surface of Fe-28Al-5Si alloy and alloys alloyed with titanium and molybdenum after cyclic oxidation are given by differences in the phase composition of tested alloys.

CONCLUSION

Long-term cyclic oxidation tests of Fe-28Al-5Si, Fe-28Al-5Si-2Ti and Fe-28Al-5Si-2Mo at 900°C and 1100°C in laboratory air were carried out, and the effect of Ti and Mo (as additive) on corrosion behaviour was evaluated. The results can be summarized in the following points:

1. The surfaces of Fe-28Al-5Si-2Ti and Fe-28Al-5Si-2Mo alloys were covered with thin and compact oxide layers during oxidation at 900°C. For both alloys, the oxide layer is com-

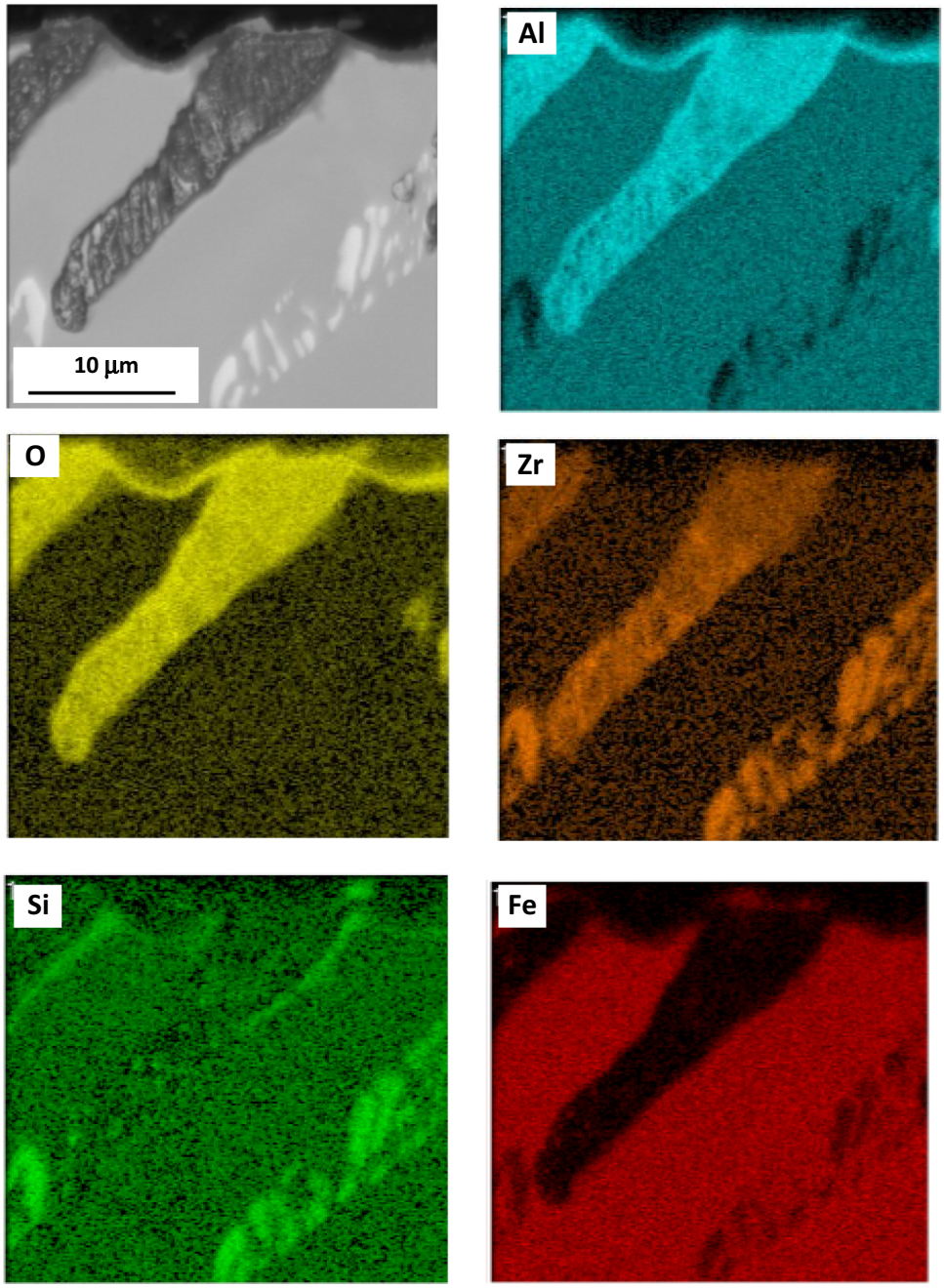

Fig. 13. SEM–EDS mapping of elements in the cross section after oxidation of Fe-28Al-5Si at 900°C.

posed mainly of α-Al_2O_3. In the case of Fe-28Al-5Si alloy, parabolic growth of weight gain has been observed. The preferential oxidation of eutectic areas is characteristic of Fe-28Al-5Si alloy. Except for α-Al_2O_3, a large amount of Fe_2O_3 was found in the oxide layer on Fe-28Al-5Si.

2. At the temperature 1100°C, oxide layer on Fe-28Al-5Si-2Ti and Fe-28Al-5Si-2Mo alloys grows approximately following the parabolic law. This oxide layer is composed only of α-Al_2O_3. The layer of alumina spalled during cyclic oxidation.
3. On the other hand, the breakaway oxidation is typical for Fe-28Al-5Si at 1100°C after 200 h. The bulk and non-protective iron-based oxides predominate on the surface (especially Fe_2O_3) of Fe-28Al-5Si.
4. The beneficial effect of Ti and Mo on the high-temperature oxidation behaviour (oxidation resistance) of alloys based on Fe-Al-Si was clearly proven. Both addition elements, titanium and molybdenum, suppress the formation of eutectic regions of the secondary phase in the structure, which preferentially oxidize, as mentioned above. Thus, the formation of a compact and protective oxide layer is enabled.

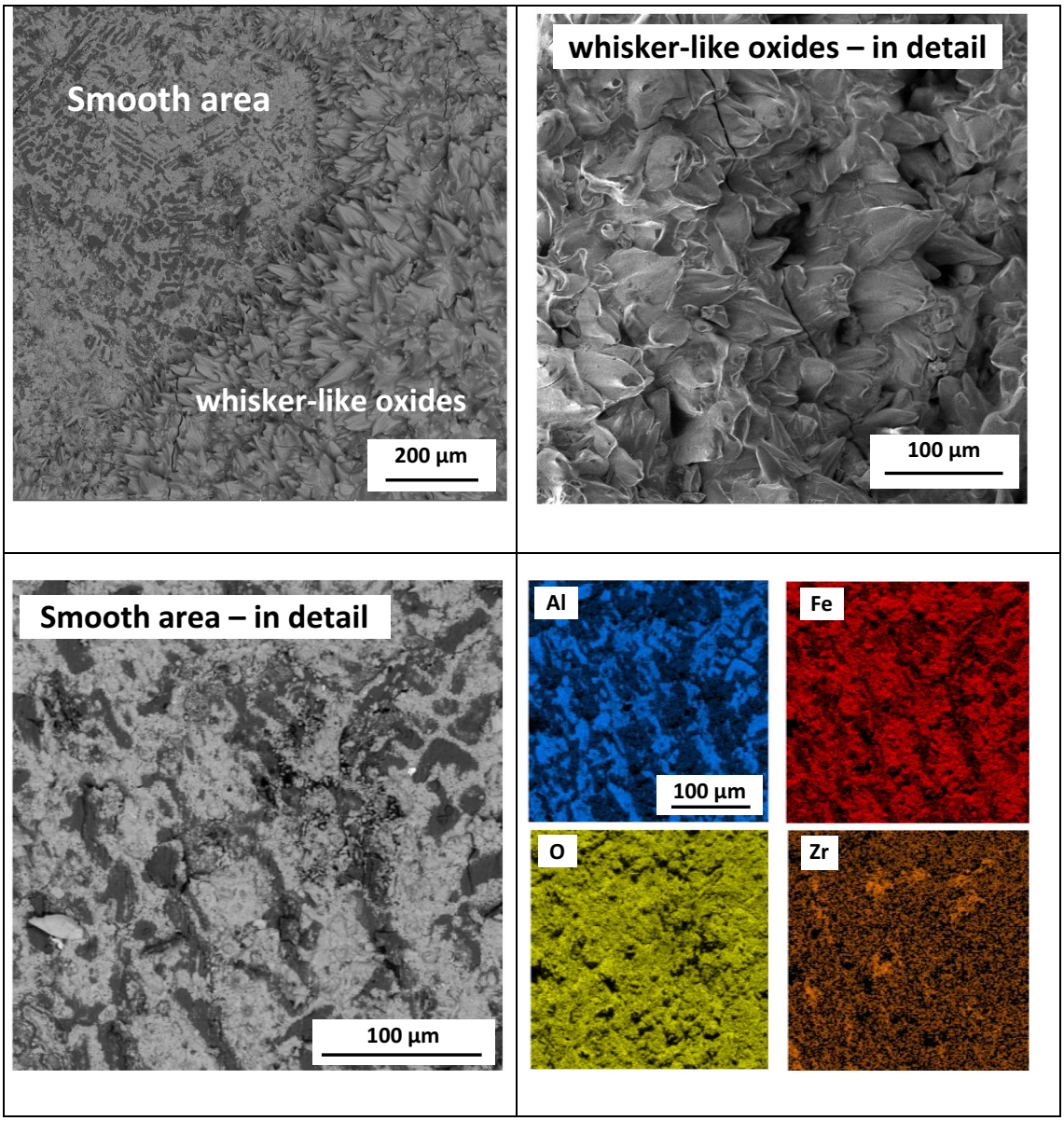

Fig. 14. Morphology of oxides on alloy Fe-28Al-5Si after oxidation at 1100°C; SEM–EDS mapping of elements of smooth area.

ACKNOWLEDGEMENTS

This research was supported by the project of the Ministry of Education, Youth and Sports of the Czech Republic and the European Union-European Structural and Investment Funds in the framework of the Operational Programme Research, Development and Education – project Hybrid Materials for Hierarchical Structures, grant HyHi, reg. no. CZ.02.1.01/0.0/0.0/16_019/0000843, and by the Institutional Endowment for the Long Term Conceptual Development of Research Institutes, as provided by the Ministry of Education, Youth and Sports of the Czech Republic in 2023.

AUTHOR CONTRIBUTIONS

Adam Hotař: Conceptualization, Oxidation tests, Writing-Original draft preparation. Věra Vodičková: XRD investigation, Writing-Reviewing and Editing. Petra Pazourková Prokopčáková: Investigation (LOM). Martin Švec: Investigation (SEM, EDS). P. Hanus: Characterisation of as-cast structure. Stanislav Daniš: Investigation (XRD).

FUNDING

Open access publishing supported by the National Technical Library in Prague.

CONFLICT OF INTEREST

The authors certify that they have no affiliations with or involvement in any organization or entity with any financial interest or non-financial interest in the subject matter or materials discussed in this manuscript.

OPEN ACCESS

REFERENCES

1. P. Kejzlar, P. Kratochvíl, R. Král and V. Vodičková, *Metall. Mater. Trans. A-Phys. Metall. Mater. Sci.* 45, 335 https://doi.org/10.1007/s11661-013-1987-1 (2014).
2. P. Kratochvíl, M. Švec, R. Král, J. Veselý, P. Lukáč and T. Vlasák, *Metall. Mater. Trans. A-Phys. Metall. Mater. Sci.* 49, 1598 https://doi.org/10.1007/s11661-018-4524-4 (2018).
3. M. Palm, *Intermetallics* 13, 1286 https://doi.org/10.1016/j.intermet.2004.10.015 (2005).
4. P. Novák, K. Nová, T. Vanka and F. Průša, *Manuf. Technol.* 18, 299 (2018).
5. K. Nová, P. Novák, A. Arzel and F. Průša, *Manuf. Technol.* 18, 645 (2018).
6. P. Novák, V. Knotek, M. Voděrová, J. Kubásek, J. Šerák, A. Michalcová and D. Vojtěch, *J. Alloy. Compd.* 497, 90 https://doi.org/10.1016/j.jallcom.2010.03.028 (2010).
7. P. Novák, A. Lamchaouri, K. Nová and F. Průša, *Manuf. Technol.* 19, 660 (2019).
8. V. Vodičková, M. Švec, P. Hanus, P. Novák, A. Záděra, V. Keller and P.P. Prokopčáková, *Molecules* 25, 4268 https://doi.org/10.3390/molecules25184268 (2020).
9. M. Švec, V. Vodičková, P. Hanus, P.P. Prokopčáková, L. Čamek and J. Moravec, *Materials* 141, 3031 https://doi.org/10.3390/ma14113031 (2021).
10. P. Novák, M. Zelinková, J. Šerák, A. Michalcová, M. Novák and D. Vojtěch, *Intermetallics* 19, 1306 https://doi.org/10.1016/j.intermet.2011.04.011 (2011).
11. P. Novák, T. Vanka, K. Nová, J. Stoulil, F. Průša, J. Kopeček, P. Haušild and F. Laufek, *Materials* 12, 2463 https://doi.org/10.3390/ma12152463 (2019).
12. P. Novák, Z. Barták, K. Nová and F. Průša, *Materials* 13, 800 https://doi.org/10.3390/ma13030800 (2020).
13. S. Milenkovic and M. Palm, *Intermetallics* 16, 1212 https://doi.org/10.1016/j.intermet.2008.07.007 (2008).
14. P. Novák and K. Nová, *Materials* 12, 1748 https://doi.org/10.3390/ma12111748 (2019).
15. A. Hotař, V. Hotař, M. Švec and S. Daniš, *Oxid. Met.* 98, 77 https://doi.org/10.1007/s11085-022-10111-9 (2022).
16. A. Hotař, M. Palm, P. Kratochvíl, V. Vodičková and S. Daniš, *Corros. Sci.* 63, 71 https://doi.org/10.1016/j.corsci.2012.05.027 (2012).
17. R. Prescott, M.J. Graham, H. Köhne, K. Lucka, S. Richter and J. Mayer, *Oxid. Met.* 38, 233 https://doi.org/10.1007/BF00666913 (1992).
18. S. Chevalier, P. Juzon, G. Borchardt, A. Galerie, K. Przybylski and J.P. Larpin, *Oxid. Met.* 73, 43 https://doi.org/10.1007/s11085-009-9168-8 (2010).
19. K. Wambach, J. Peters and H.J. Grabke, *Mater. Sci. Eng. A-Struct. Mater. Prop. Microstruct. Process.* 88, 205 https://doi.org/10.1016/0025-5416(87)90086-3 (1987).
20. N.I. Jamnapara, D.U. Avtani, N.L. Chauhan, P.M. Raole, S. Mukherjee and A.S. Khanna, *Surf. Eng.* 28, 693 https://doi.org/10.1179/1743294412Y.0000000046 (2012).
21. A. Hotař and M. Palm, *Intermetallics* 18, 1390 https://doi.org/10.1016/j.intermet.2010.02.014 (2010).
22. P. Brito, H. Pinto and A. Kostka, *Corros. Sci.* 105, 100 https://doi.org/10.1016/j.corsci.2016.01.007 (2016).
23. D. Janda, H. Fietzek, M. Galetz and M. Heilmaier, *Intermetallics* 41, 51 https://doi.org/10.1016/j.intermet.2013.04.016 (2013).
24. H.J. Grabke, *Intermetallics* 7, 1153 https://doi.org/10.1016/S0966-9795(99)00037-0 (1999).
25. G.C. Rybicki and J.L. Smialek, *Oxid. Met.* 31, 275 https://doi.org/10.1007/BF00846690 (1989).
26. S.P. Gupta, *Mater. Charact.* 49, 269 https://doi.org/10.1016/S1044-5803(03)00006-8 (2002).
27. T. Maintra and S.P. Gupta, *Mater. Charact.* 49, 293 https://doi.org/10.1016/S1044-5803(03)00005-6 (2002).
28. L.F. He, Y.C. Zhou, Y.W. Bao, J.Y. Wang and M.S. Li, *Int. J. Mater. Res.* 98, 3 https://doi.org/10.3139/146.101427 (2007).
29. J.M. Guilemany, N. Cinca, S. Dosta and C.R.C. Lima, *Intermetallics* 15, 1384 https://doi.org/10.1016/j.intermet.2007.04.013 (2007).
30. A.I.O. Zaid and A.M. Atieh, *IOP Conf. Ser. Mater. Sci. Eng.* 60, 012052 https://doi.org/10.1088/1757-899X/60/1/012052 (2014).
31. C.G. McKamey and J.A. Horton, *Metall. Mater. Trans. A* 20A, 751 https://doi.org/10.1007/BF02667592 (1989).
32. A. Hotař, P. Kratochvíl and J. Cízner. In *METAL 2010 - 19th International Conference on Metallurgy and Materials*, 915 (2010) Ostrava: TANGER.
33. R.D. Pütz and D. Zander, *Corros. Sci.* 198, 110149 https://doi.org/10.1016/j.corsci.2022.110149 (2022).